



HAL
open science

Kinetic studies of hydrothermal carbonization of avocado stone and analysis of the polycyclic aromatic hydrocarbon contents in the hydrochars produced

Diakaridia Sangare, Agnes Chartier, Mario Moscosa-Santillan, Iskender Gökalp, Stéphane Bostyn

► To cite this version:

Diakaridia Sangare, Agnes Chartier, Mario Moscosa-Santillan, Iskender Gökalp, Stéphane Bostyn. Kinetic studies of hydrothermal carbonization of avocado stone and analysis of the polycyclic aromatic hydrocarbon contents in the hydrochars produced. *Fuel*, 2022, 316, pp.123163. 10.1016/j.fuel.2022.123163 . hal-03812199

HAL Id: hal-03812199

<https://cnrs.hal.science/hal-03812199v1>

Submitted on 22 Jul 2024

HAL is a multi-disciplinary open access archive for the deposit and dissemination of scientific research documents, whether they are published or not. The documents may come from teaching and research institutions in France or abroad, or from public or private research centers.

L'archive ouverte pluridisciplinaire **HAL**, est destinée au dépôt et à la diffusion de documents scientifiques de niveau recherche, publiés ou non, émanant des établissements d'enseignement et de recherche français ou étrangers, des laboratoires publics ou privés.



Distributed under a Creative Commons Attribution - NonCommercial 4.0 International License

1 **Kinetic Studies of Hydrothermal Carbonization of Avocado Stone and**
2 **Analysis of the Polycyclic Aromatic Hydrocarbon Contents in the Hydrochars Produced.**

3 Diakaridia Sangare^{1,2}, Agnes Chartier⁴, Mario Moscosa-Santillan¹, Iskender Gökalp², Stéphane
4 Bostyn^{2,3,*}

5 ¹ Facultad de Ciencias Químicas Universidad Autónoma de San Luis Potosí Av. Dr. Nava # 6, Zona
6 Universitaria San Luis Potosí, S.L.P., CP: 78210, México

7 ² Institut de Combustion, Aérothermique, Réactivité, et Environnement (ICARE)-CNRS UPR3021, 1C avenue
8 de la recherche scientifique 45071 Orléans Cedex 2, France

9 ³ Université d'Orléans, Institut Universitaire de Technologie, 16 rue d'Issoudun BP16724 45067 Orléans Cedex
10 2, France

11 ⁴Institut de Chimie Organique et Analytique (ICOA), Université d'Orléans-CNRS, 8 Rue de Chartres BP 6759,
12 45067 Orléans cedex 2, France

13 * Correspondence: Email: stephane.bostyn@univ-orleans.fr; Tel: +33238255476; Fax: +33238696004.

14
15 **Abstract:**

16 Model-free and model-fitting kinetic approaches were used to investigate the hydrothermal
17 carbonization (HTC) of avocado stone. The total solid mass yield was used to estimate the
18 kinetic parameters and reaction mechanism. The results obtained show that the HTC process for
19 avocado stones could be divided into four temperature zones. Up to 160 °C, the initial induction
20 period where the reaction rate is relatively slow. The second zone (160 to 200 °C) corresponds to
21 the maximum decomposition rate. The third zone between 200 and 220 °C corresponds to the
22 stabilization zone; in this zone, the total solids yield is practically constant, and finally, the
23 polymerization zone, between 220 and 250 °C, where an increase in total solid yield was
24 observed. The kinetic parameters and reaction mechanism were determined in two temperature
25 zones, from 150 to 210 °C and 210 to 250 °C. In the first zone, the decomposition of avocado
26 stone during the HTC process followed a random nucleation reaction mechanism (Avrami-
27 Erofeev-1) with the activation energy of 87.84 ± 3.28 kJ/mol. In contrast, in the second zone, it
28 followed a first-order reaction model, and the activation energy was 230.96 ± 28.84 kJ/mol.
29 Analysis of PAHs with gas chromatography-mass spectrometry showed that the number of PAHs
30 in the hydrochar increases with an increase in temperature from 190 to 250 °C. The 3-4 rings

31 PAHs were dominant in the hydrochars prepared at temperatures between 230 and 250 °C, while
32 two rings were largely prevalent in the hydrochar obtained at low temperatures.

33

34 **Keywords:** Avocado stone; hydrothermal carbonization; Kinetic model; PAHs

35 **1 INTRODUCTION**

36 The increasing demand for energy and the rapid depletion of fossil fuels are the reasons for
37 the need to find new sources of energy, sustainable technologies, or processes that are
38 environmentally friendly. This problem has inspired researchers to study and develop more
39 efficient and reliable tools to exploit biomass as a source of renewable energy. The
40 thermochemical conversion processes of biomass have better industrial prospects for biomass
41 valorization since the process conditions can be optimized to maximize gas, liquid, and solid
42 yields [1]. Among thermochemical processes, hydrothermal carbonization (HTC) of biomasses
43 (agro-industrial, forestry, and urban waste) has received widespread attention in recent years
44 because of its efficiency and convenience [2, 3]. HTC technology is based on a thermochemical
45 conversion process by which it converts organic material into carbonized material (hydrochar),
46 liquid (bio-oil mixed with water), and small fractions of gases. The HTC process is performed in
47 the temperature range of 180-250°C, during which biomass is submerged in water and is heated
48 under autogenous saturated vapor pressure between 10 and 40 bars and residence time ranging
49 from a few minutes up to several hours [4]. Under these process conditions, water exhibits a
50 behavior similar to that of an organic solvent owing to changes in its polarity and dielectric
51 constant and acts as a catalyst for the conversion of biomass through hydrolysis, dehydration,
52 decarboxylation, aromatization, condensation, and polymerization [5]. Through the HTC
53 process, researchers have investigated distinct types of biomass, tomato waste [6], sugarcane
54 bagasse [7], olive pomace [4], corn cob [8], and olive stones [9]. Most of these biomasses are
55 agro-industrial wastes. Avocado stones is some of the most massive agro-industrial wastes
56 generated in Mexico.

57 The avocado is one of the most frequently consumed fruits in the world. Mexico is globally the
58 leading avocado producing country, with more than 45% (~2.18 million tons/year) of the total
59 production in 2020 [10]. Products derived from avocados include ice cream, drinks, and

60 guacamole being the most marketed product [11]. There are also examples of avocado oil
61 production, which is of a quality similar to olive oil [12]. Avocado processing generates an
62 enormous amount of waste, particularly the skin and seed or stone. The stone represents 15.0–
63 16.0% of the fruit weight [13]. A significant amount (~170,000 tons/year) of avocado production
64 is guacamole, and this represents more than 25,000 tons of waste per year [14].

65 The technology of the HTC process of waste to form hydrochar and bio-oil has been is the focus
66 in recent years [6, 8, 9]. During the HTC process, hydrochar formation can be carried out in two
67 reaction pathways. The formation can proceed from the reaction of the solid-solid pathway
68 known as primary hydrochar (P-HC), in which hydrochar maintains the original structural
69 elements and morphology of the parent biomass matrix; and the hydrochar formation can be
70 carried out from aqueous phase degradation of the biomass followed by polymerization of the
71 organic molecules into a solid phase, called secondary hydrochar (S-HC). This secondary
72 hydrochar is extractable with organic solvents [15]. This S-HC is a sequential result of
73 hydrolysis, dehydration, and isomerization during HTC to produce furfurals and their
74 derivatives. The furfurans and their derivatives polymerize as microspheres, these microspheres
75 can be further carbonized by dehydration reactions, resulting in an amorphous solid that is
76 soluble in organic solvents [15]. Although, Paksung et al.[16] reported that it is not easy to
77 distinguish analytically between P-HC and S-HC; because both appear as a single solid mass of
78 char.

79 The main product of HTC is hydrochar, a solid material 55-74% rich in carbon, is the stable, a
80 lignite-like material which is characterized by a high heating value (21.1–30.6 MJ/kg) [4] and its
81 physical, chemical, and mechanical properties make it susceptible to different uses. Hydrochar
82 can thus be used directly as a solid fuel that can be burned for energy or produce syngas. Most
83 recently, the hydrochar has also been applied as an additive agent for soil amendment [17, 18].
84 The hydrochar has proved to be a favorable soil of amendment, increased cation extraction
85 capacity, and reduced solid bulk density [19]. However, for the soil use of hydrochars,
86 contaminants such as heavy metals and polycyclic aromatic hydrocarbons (PAHs), in hydrochars
87 are of significant concerns.

88 Peng et al. [17] reported a significant increase of PAHs in the hydrochar of municipal solid
89 waste, with the increase in temperature of HTC between 160°C and 240°C. The formation of

90 PAHs from biomass is -a multi-step process. The S-HC formation during the hydrothermal
91 carbonization of biomass leads to increased PAHs formation and their retention in the primary
92 hydrochar [20, 21].

93 Biomass decomposition by HTC is dominated by chemical reactions similar to pyrolysis;
94 however, the HTC process is initiated by hydrolysis, leading to biomass decomposition
95 temperatures lower than those of pyrolysis [23]. The HTC reaction mechanisms complexity has
96 led some authors to develop lumped kinetics models to describe it [24]. For simplification, the
97 authors have used the biomass components model, such as cellulose, hemicellulose, and lignin.
98 For example, Reza et al. [25] determined the activation energy of cellulose and hemicellulose in
99 the temperature range between 200 and 260°C. They reported that cellulose degradation is
100 described by a first-order rate constant with an activation energy 73 ± 6 kJ/mol, and hemicellulose
101 degradation has an activation energy of 30 ± 12 kJ/mol. For the same operating conditions (200-
102 260°C), Killer et al. [26] reported activation energy values equal to 61 kJ/mol and 127 kJ/mol for
103 hemicellulose and cellulose, respectively. On the other hand, Liu and Balasubramanian [27]
104 considered the HTC process as a first-order reaction and estimated the activation energy for
105 coconut fibers (67.5 kJ/mol) and eucalyptus leaves (59.2 kJ/mol). Recently Pecchi et al. [28]
106 reported E_a values of 139.16 and 161.68 kJ/mol and reaction orders of about 2.68 and 2.46, for
107 digestate and sludge, respectively, using Differential Scanning Calorimetry. As can be seen,
108 different approaches have been used to determine the kinetic parameters during the HTC process
109 of the biomass. However, researchers have used conventional methods in only a few studies to
110 determine kinetic parameters. Methods based on thermal analysis, such as thermogravimetric
111 analysis, have been widely used in the literature to study biomass decomposition kinetics. They
112 are high-precision methods that can be used for the quantitative examination of processes as well
113 as for estimating useful kinetic parameters for various thermal decomposition reactions. Since
114 thermogravimetric analysis is a technique based on mass loss or conversion as a function of
115 temperature and time during thermochemical conversion, a similar analogy can be used for the
116 HTC process based on the hydrochar mass yield as a function of temperature and reaction time.

117 For this reason, this research - focuses on the determination of the kinetic parameters that
118 described the hydrothermal carbonization process of the avocado stone, using the thermal
119 analysis technique in an open-loop controller system. The biomass's HTC behavior was studied
120 using the total solid mass yield or hydrochar yield produced at different temperatures and times.

121 The kinetic predictions were made by using the Model-Free Method, such as FWO, KAS, and
 122 Friedman and the Model-Fitting Methods were used to determine the most appropriate kinetic
 123 model mechanism of HTC reactions. In addition, a qualitative analysis of the hydrochars
 124 produced was performed to determine the structure of polycyclic aromatic hydrocarbons (PAHs).

125 2 MATERIALS AND METHODS

126 2.1 Feedstock

127 In this study, avocado stones (AS) of the *Hass* variety from Michoacán (Mexico) were used. In
 128 general, an AS has a moisture content between 65 and 75% [29], which is ideal for HTC.
 129 Initially, an AS was cut and dried in a stove at 80 °C for storage; subsequently, it was ground to
 130 obtain a particle size between 0.5 and 1mm. **Table 1** contains the physical and chemical
 131 characteristics associated with the raw AS. The details of the determination of these parameters
 132 were explained in our previous study [30].

133 **Table 1.** Proximate, ultimate, extractive, hemicellulose, cellulose, lignin analysis, and higher heating
 134 value characteristics of AS

Proximate analysis (%)	
MC	3.2±0.4
VM	72.5±1.7
FC ^a	22.4±1.0
Ash	1.9±0.6
Ultimate analysis (%)	
Carbon	46.1±0.2
Hydrogen	6.4±0.1
Nitrogen	0.02 ± 0.0
Sulphur	nd
Oxygen ^a	47.9±0.9
Extractives (%)	3.6±0.4
Hemicellulose (%)	76.4±0.3
Cellulose ^a (%)	3.0±0.3
Lignin (%)	17.0±0.3
HHV(MJ/kg)	18.6±0.2

MC: moisture content; VM: volatile matter; FC: fixed carbon; nd: not detected; ^a:by difference

135 2.2 HTC Reactor Description and Experimental Procedure

136 The detailed descriptions of the experimental procedures can be found in our previous studies
 137 [31]. Briefly, the HTC experiments were carried out in the stirred autoclave reactor (Top
 138 Industrie, France) with an internal volume of 300 mL suitable for a pressure of 100 bars. This
 139 stirred autoclave reactor consisted of a reactor vessel and a cylindrical capping vessel. The

140 capping vessel included a central connection for a magnetic stirrer (max. 1500rpm, 50 W) and
141 connections for measuring pressure, monitoring temperatures, and releasing the gases. For each
142 HTC run, 18.65 ± 0.05 g of dry sample were loaded into the reactor together with 186.5 ± 1.5 g of
143 deionized water, with a biomass-to-water ratio (AS/W) equal to 1/10 (w/w). Before starting the
144 heating program, the residual air inside the reactor was removed using a vacuum pump to a
145 pressure of less than 40 mbar. The reactor was heated from room temperature to setpoint
146 temperature at different powers supplied in the reactor 160, 200, and 240 W; these represent
147 overall average heating rate of 1.5, 2.0, and 2.8 °C/min, respectively. The setpoint temperature
148 was varied from 150 °C to 250 °C. For powers of 160 and 240 W, the setpoint temperatures were
149 150, 170, 190, 210, 230 and 250 °C, while for power of 200 W the setpoint temperatures were
150 150 to 250 °C with a 10 °C increase. The setpoint temperatures of 150, 190, and 250 °C were
151 carried out in triplicate; allowing to define an error less than 1.5% in all cases. During the
152 experiment, the reactor was stirred at 550 rpm. After the reactor reaches the setpoint temperature,
153 it was immediately cooled down, and this took 5 to 10 minutes to cool it down by immersing it in
154 a 5 °C water bath. After cooling the reactor, the system pressure was noted, the reactor was
155 opened, the liquid and solids were separated with a Whatman filter paper with a pore size of 11
156 microns, and the solid was weighed after drying at 105 °C for 24 hours in the stove. The
157 hydrochar yield or total solid yield (Y_{HC}) was determined through the **Eq.(1)**:

$$Y_{HC} = \frac{m_{HC}}{m_{bio}} \cdot 100 \quad (1)$$

158 Where m_{HC} is the mass of total solid (on a dry base), and m_{bio} is the raw biomass mass (on a dry
159 base). The derivative hydrochar yield (DY_{HC}) is the first-order derivative of Y_{HC} with respect to
160 time. From this approach, it is possible to determine the maximum temperature decomposition of
161 biomass. The DY_{HC} was determined through the **Eq.(2)**:

$$DY_{HC} = \frac{\Delta Y_{HC}}{\Delta t} \quad (2)$$

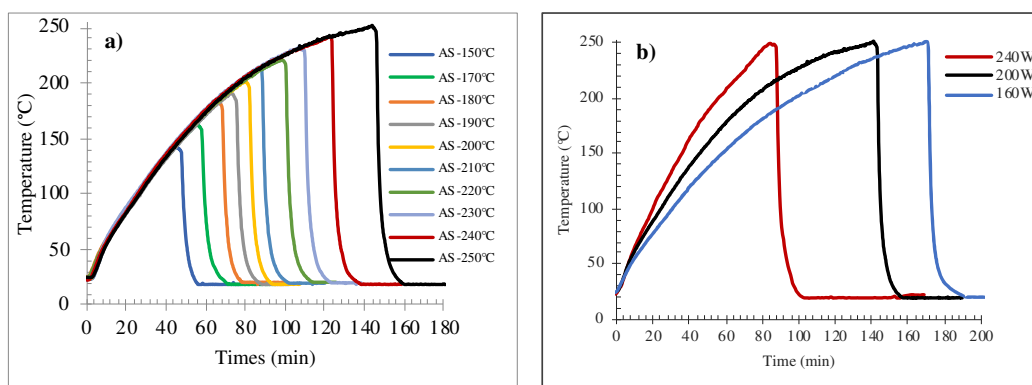
162 Where DY_{HC} is derivative hydrochar yield (%/min), ΔY_{HC} is the difference between Y_{HC} from
163 one setpoint temperature to another, and Δt is the time variation (min) between setpoint
164 temperatures.

165 **2.3 HTC reactor heat-up and reaction time**

166 In reality, the constant temperature during HTC is not correct in batch autoclave reactors because
167 there are different step of heating: i) a heating time, ii) a holding time temperature, and finally,

168 iii) a cooling time. In many publications in the literature, the definition of reaction time is not
169 standardized. Often, HTC reaction time starts to be counted when the set HTC temperature is
170 reached [4] while in some other cases [32] includes heat-up time. The heat-up time may be
171 neglected only if it is very rapid as it could be the case when the HTC is performed in batch
172 micro-reactors. In this study, an open-loop system was used, where the power supplied to the
173 furnace of the reactor is controlled (i.e., constant in each experiment), and we consider the
174 reaction time of the HTC is the heat-up time until the setpoint temperature is reached.

175 **Fig. 1** shows the different heating time profiles established for different setpoint temperatures at
176 200 W electrical power (**Fig. 1a**) and for the different electrical powers used (**Fig. 1b**). In this
177 case, holding time temperature and cooling time was not considered because when the setpoint
178 temperature was reached, the reactor was cold down from setpoint temperature to room
179 temperature; it took 5 to10 minutes to cool it down by immersing it in a 5°C water bath.



180

181 **Fig. 1:** Temperature trends vs. time of hydrothermal tests, (a) conducted at 200W to set-point
182 temperature, (b) different powers (heating rate) from ambient temperature to 250 °C.

183

184 2.4 Secondary hydrochar extraction and GC–MS analyzer

185 Extraction of S-HC was performed with toluene (100%) as the extraction solvent in a Soxhlet
186 extractor. Toluene is a good solvent for the extraction of tar, such as PAHs, in hydrochar [33].

187 For each extraction, about 2 g of hydrochar and 250 mL toluene were placed in the Soxhlet
188 extractor for 36 h. After this time, the solution was concentrated by a rotary evaporator to obtain
189 25 mL volume. The S-HC composition was detected using a GC–MS analyzer. The analysis was
190 carried out by two different methods and columns to detect aliphatic and PAHs compounds.

191 Aliphatic compounds were detected on a Trace Ultra-ISQ gas chromatograph single quadrupole
192 mass spectrometer (Thermo Scientific, Villebon Sur Yvette, France) equipped with a

193 programmed temperature vaporizing injector (PTV) and a 2 mm diameter. Thermo PTV liner
194 was used. A DB35ms column (30 m length, 0.25 mm internal diameter, and 0.25 μm film
195 thickness) was installed in the GC oven. Initially the temperature of the GC oven was set at 80
196 $^{\circ}\text{C}$ for 2 min followed by a 10 $^{\circ}\text{C}/\text{min}$ ramp to 200 $^{\circ}\text{C}$ and a 15 $^{\circ}\text{C}/\text{min}$ ramp to 320 $^{\circ}\text{C}$ with a 5
197 min hold. For the data acquisition using the Electron Impact (EI) mode, the transfer line
198 temperature and the ion source were held at 315 $^{\circ}\text{C}$ and 250 $^{\circ}\text{C}$, respectively. A mass range (m/z
199 50–300 amu with a dwell time of 0.2s) was scanned in full scan acquisition. In order to detect
200 PAHs, the extracted liquid was diluted 50 times in dichloromethane. The PAHs were detected on
201 a Trace Ultra gas chromatography coupled with a quadrupole mass spectrometer. A DB17ms
202 Agilent column (30 m length, 0.32 mm internal diameter, and 0.25 μm film thickness) was
203 installed in the GC oven. Initially, the temperature of the GC oven was set at 40 $^{\circ}\text{C}$ for 7 min
204 followed by a 20 $^{\circ}\text{C}/\text{min}$ ramp to 75 $^{\circ}\text{C}$, and it was held on for 15 minutes and then a 20 $^{\circ}\text{C}/\text{min}$
205 ramp to 200 $^{\circ}\text{C}$ for 8 minutes, and finally a 10 $^{\circ}\text{C}/\text{min}$ ramp to 220 $^{\circ}\text{C}$, and it was held on for 55
206 minutes. For the data acquisition using the Electron Impact (EI) mode, both the temperature of
207 the transfer line and the ion source was held at 200 $^{\circ}\text{C}$. The temperature for the inlet injector was
208 fixed at 300 $^{\circ}\text{C}$ for attaining a well-vaporization of the sample, and a spitless liner was installed.
209 A mass range (m/z) of 50–300 amu was scanned, that is, in full scan acquisition.

210 **2.5 Kinetic models and mechanisms of the HTC process of biomass**

211 A model is a theoretical and mathematical description of what occurs experimentally. This study
212 will analyze the kinetic models that can describe the kinetic reaction of the HTC process of the
213 biomass, based only on the formation of hydrochar (evolution of the solid phase). The overall
214 reaction of the biomass in the HTC process is presented in the following reaction:



215 The mass yield of the solid or hydrochar produced during HTC for time ($d\alpha/dt$), depends on the
216 rate of reaction constants, which are influenced by temperature [$k(T)$] and reaction model [$f(\alpha)$],
217 expressed as:

$$\frac{d\alpha}{dt} = k(T) \cdot f(\alpha) \quad (4)$$

218 where $k(T)$ is the reaction rate constant depending on the temperature, $f(\alpha)$ is the function of α ,
219 and α is the conversion or weight loss rate that can be calculated with the following equation:

$$\alpha = \frac{m_{\text{bio}} - m_{\text{HC}_T}}{m_{\text{bio}} - m_{\text{HC}_\infty}} \quad (5)$$

220 where m_{bio} (g), is the initial weight of the sample, m_{HC_T} (g) is the weight of the sample at a
 221 given temperature and time, and m_{HC_∞} (g) is the final sample weight. The solid conversion rate
 222 ($d\alpha/dt$) can be expressed as:

$$\frac{d\alpha}{dt} = \beta \frac{d\alpha}{dT} = k(T) \cdot f(\alpha) \quad (6)$$

223 where β is the heating rate or the rate of temperature change (dT/dt , K/min).

224 The kinetic parameters were determined using two HTC temperature zones (150-210 °C and
 225 210-250 °C). For each temperature range, the biomass samples were subjected to three heating
 226 powers (160, 200 and 240 W). These powers correspond to different average value of β
 227 depending on the temperature zone. In the first zone, the β values corresponding to the powers
 228 were 1.8, 2.3 and 3 °C/min, while in the second zone the β values were 0.7, 1.25 and 1.8 °C/min.
 229 The continuous decrease of β value for the duration of the experiment at the same power is due
 230 to heat loss. However, for each power in the given temperature range, the value of β can be
 231 considered constant. As shown in **Fig. 1**, the temperature profile as a function of time at 150-210
 232 °C; and 210-250 °C, can be considered as straight lines with $R^2 > 0.983$ for each.

233 The $k(T)$ can be described according to the Arrhenius equation:

$$k(T) = A \cdot e^{\frac{-E\alpha}{RT}} \quad (7)$$

234 where A (min^{-1}) refers to the pre-exponential factor, and $E\alpha$ (J/mol) is the apparent activation
 235 energy, T (K) represent the absolute temperature, and R universal gas constant (8.314 J/
 236 ($\text{mol} \cdot \text{K}$)), respectively. Substituting Eq. (7) into (6) gives the following equation:

$$\frac{d\alpha}{dt} = \beta \frac{d\alpha}{dT} = A \cdot e^{\frac{-E\alpha}{RT}} \cdot f(\alpha) \quad (8)$$

237 The integral form of $f(\alpha)$ can be obtained after integrating Eq. (8) with respect to temperature.

$$g(\alpha) = \int_0^\alpha \frac{d\alpha}{f(\alpha)} = \frac{A}{\beta} \int_{T_0}^T e^{\frac{-E\alpha}{RT}} dT \quad (9)$$

238 where $g(\alpha)$ is the integrated reaction model, and some common forms of $f(\alpha)$ and $g(\alpha)$ for solid-
 239 state reactions are described in **Table 2**.

240 **Table 2:** Expressions for functions $f(\alpha)$ and $g(\alpha)$ of some reaction models to describe thermal
 241 decomposition solid state reactions [34]

Symbols	Reaction models	Differential form $f(\alpha)$	Integral form $g(\alpha)$
		Reaction order models	

R1	First order	$1 - \alpha$	$-\ln(1 - \alpha)$
R2	Second order	$(1 - \alpha)^2$	$(1 - \alpha)^{-1} - 1$
R3	Third order	$(1 - \alpha)^3$	$[(1 - \alpha)^{-2} - 1]/2$
R4	One and half order	$(1 - \alpha)^{3/2}$	$[(1 - \alpha)^{-1/2} - 1]$
Diffusion models			
D1	1D diffusion	$1/2\alpha$	α^2
D2	2D diffusion-Valensi	$[-\ln(1 - \alpha)]^{-1}$	$(1 - \alpha)\ln(1 - \alpha) + \alpha$
D3	3D diffusion-Jander	$(1 - \alpha)^{3/2}/[1 - (1 - \alpha)^{1/3}]$	$[1 - (1 - \alpha)^{1/3}]^2$
D4	3D diffusion-Ginstling	$(3/2)/[(1 - \alpha)^{-1/3} - 1]$	$1 - 2\alpha/3 - (1 - \alpha)^{2/3}$
Power law nucleation Models			
P1	Power law (1)	$(2/3)\alpha^{-1/2}$	$\alpha^{3/2}$
P2	Power law (2)	$2\alpha^{1/2}$	$\alpha^{1/2}$
P3	Power law (3)	$3\alpha^{2/3}$	$\alpha^{1/3}$
P4	Power law (4)	$4\alpha^{3/4}$	$\alpha^{1/4}$
Random nucleation and subsequent growth Models			
A1	Avrami-Erofeev (1)	$(3/2)(1 - \alpha)[- \ln(1 - \alpha)]^{1/3}$	$[- \ln(1 - \alpha)]^{2/3}$
A2	Avrami-Erofeev (2)	$2(1 - \alpha)[- \ln(1 - \alpha)]^{1/2}$	$[- \ln(1 - \alpha)]^{1/2}$
A3	Avrami-Erofeev (3)	$3(1 - \alpha)[- \ln(1 - \alpha)]^{2/3}$	$[- \ln(1 - \alpha)]^{1/3}$
A4	Avrami-Erofeev (4)	$4(1 - \alpha)[- \ln(1 - \alpha)]^{3/4}$	$[- \ln(1 - \alpha)]^{1/4}$
A5	Random nucleation (1)	$(1 - \alpha)^2$	$1/(1 - \alpha)$
A6	Random nucleation (2)	$(1 - \alpha)^3/2$	$1/(1 - \alpha)^2$
Geometrical contraction models			
F1	Contracting area	$2(1 - \alpha)^{1/3}$	$1 - (1 - \alpha)^{1/2}$
F2	Contracting volume	$3(1 - \alpha)^{2/3}$	$1 - (1 - \alpha)^{1/3}$

242 The kinetics of thermal reactions in solids has been widely studied in the literature [34]. There
 243 are two main methods to determine the kinetic parameters, the model-free methods, and the
 244 model-fitting method.

245 2.5.1 Model-free method

246 The model-free method has been used in the pyrolysis, gasification, and combustion kinetic
 247 model and allows the kinetic parameters to be calculated as a function of the degree of
 248 conversion. Different methods have been used, such as the differential method proposed by
 249 Friedman and the integral methods, such as the FWO method and KAS method [46-48].

250 *Friedman method:* The Friedman method is the most common differential isoconversion method
 251 for determining activation energy as a function of conversion α , and it is given in the following
 252 equation:

$$\ln\left(\frac{d\alpha}{dt}\right) = \ln\left(\beta \frac{d\alpha}{dt}\right) = \ln[A_\alpha f(\alpha)] - \frac{E\alpha}{RT} \quad (10)$$

253 E_a can be obtained from the slope of the fit line drawn between $\ln\left(\beta \frac{d\alpha}{dt}\right)$ versus $\frac{1}{T}$.

254 *FWO method:* This method is derived from the integral isoconversional method. The method
 255 uses the linear Doyle's approximation for the estimation of temperature integral [35], and it is
 256 given in the following equation:

$$\ln \beta = \ln \frac{AE\alpha}{Rg(\alpha)} - 5.331 - 1.052 \frac{E\alpha}{RT} \quad (11)$$

257 Plots of $\ln \beta$ vs. $1/T$, at fixed value of conversion help in evaluating the activation energy from
 258 the slope of straight-line plot.

259 *KAS method:* The KAS method is based on the Coats–Redfern approximation and it is given in
 260 the following equation:

$$\ln \frac{\beta}{T^2} = \ln \frac{AR}{E\alpha g(\alpha)} - \frac{E\alpha}{RT} \quad (12)$$

261 For a constant value of α , the activation energy $E\alpha$ can be obtained from the plot of $\ln \frac{\beta}{T^2}$ against
 262 $\frac{1}{T}$ with $-E\alpha/R$ as the slope.

263 Several solid-state kinetic models have been discussed in the literature, and many different
 264 reaction mechanisms have been proposed to describe solid-state reactions, some of which are
 265 listed in **Table 2**. The models can be expressed in a differential form $f(\alpha)$ and an integral form
 266 $g(\alpha)$. The most used reaction mechanisms are described below.

267 2.5.2 Model-fitting methods

268 Model-fitting methods are commonly applied because the kinetic parameters can be determined
 269 and provide information about possible reaction mechanism models. The Coats-Redfern method,
 270 the most popular form of model-fitting, proposed in 1964 [36], uses Taylor's series approach by
 271 limiting the number of terms in the series. The Taylor series expansion form can be given as:

$$g(\alpha) = \int_0^\alpha \frac{d\alpha}{f(\alpha)} = \frac{A}{\beta} \int_{T_0}^T e^{-\frac{E\alpha}{RT}} dT = \frac{AE\alpha}{\beta R} \int_x^\infty \frac{e^{-x}}{x^2} dx \quad (13)$$

$$g(\alpha) = \frac{AE\alpha}{\beta R} \int_x^\infty \frac{e^{-x}}{x^2} dx \cong \frac{AE\alpha}{\beta R} \left[\frac{e^{-x}}{x^2} \left(1 - \frac{2!}{x} + \frac{3!}{x^2} - \frac{4!}{x^3} + \dots \right) \right] \quad (14)$$

$$\frac{AE\alpha}{\beta R} \left[\frac{e^{-x}}{x^2} \left(1 - \frac{2!}{x} + \frac{3!}{x^2} - \frac{4!}{x^3} + \dots \right) \right] = \frac{AE\alpha}{\beta R} p(x) \quad (15)$$

272 where x is equal to $\frac{E\alpha}{RT}$, the $p(x)$ is the temperature integral and it has no analytical solution.

273 Therefore, **Eq. (15)** can only be solved using either numerical integration or approximation to
 274 deal with the complex integral. By introducing an approximation $p(x) = x^{-2}e^{-x}$ ($20 \leq x \leq 50$) into
 275 **Eq. (14)**, the relationship between heating rate and inverse temperature becomes:

$$g(\alpha) = \frac{ART^2}{\beta E\alpha} \left(1 - \frac{2RT}{E\alpha} \right) e^{-\frac{E\alpha}{RT}} \quad (16)$$

276 Taking the natural logarithm of both sides of **Eq. (16)**.

$$\ln \frac{g(\alpha)}{T^2} = \ln \frac{AR}{\beta E\alpha} \left(1 - \frac{2RT}{E\alpha}\right) - \frac{E\alpha}{RT} \quad (17)$$

277 Since $2RT/E\alpha \ll 1$, the equation can be converted into

$$\ln \frac{g(\alpha)}{T^2} = \ln \frac{AR}{\beta E\alpha} - \frac{E\alpha}{RT} \quad (18)$$

278 For a fixed β and proposed reaction mechanism $g(\alpha)$, plotting $\ln \frac{g(\alpha)}{T^2}$ versus $\frac{1}{T}$ gives a straight
 279 line. The equations corresponding to $g(\alpha)$ are presented in **Table 2**. The slope $-E\alpha/R$ and
 280 intercept $\ln \frac{AR}{\beta E\alpha}$ can be used to determine $E\alpha$ and A , respectively [37].

281 **2.5.3 Kinetic reaction mechanism models**

282 All kinetic reaction mechanism models used in this study are presented in **Table 2**. Most solids
 283 contain different defects, weak points that can initiate physical and chemical changes during their
 284 reaction. These defects play an essential role when nucleation is the limiting step in a reaction
 285 [38]. If the reaction involves random nucleation followed by the growth of nuclei of a defined
 286 dimensionality, the Avrami-Erofeev equation can be derived and applied; in some cases, the
 287 nucleation rate follows the power law [37, 39]. In other cases, the solid-state reactions, are
 288 controlled by diffusion of the reagents or products. This situation is not common because the
 289 mass transfer in the solid-state is slower [39, 40]; however, in HTC processes, where one of the
 290 most important reactions is hydrolysis [23, 41], which modifies the biomass structure, the
 291 diffusion of water into the pores of the biomass particles can control the reaction mechanisms.
 292 This phenomenon was explained by Reza et al. [42]. Some solid-state reactions involve two or
 293 more substances, where phase boundaries are formed between the reagents and the products. In
 294 this case, the advance in the phase boundary thus formed determines that reaction rate [38].
 295 When the advancement of the phase boundary is one-dimensional, a reaction of zero-order is
 296 obtained; if the phase boundary is two-dimensional the contracting area models is generated and
 297 if the phase boundary is three-dimensional, the contracting volume is obtained [43]; these
 298 models are based on the assumption of spherical solid particles. Finally, the kinetics of the solid-
 299 state reaction can be controlled by the order of the reaction. These models are the simplest as
 300 they are similar to those used in homogenous kinetics [24, 44]. Often, first and second-order
 301 reactions are used. Higher-order reactions are rarely used and difficult to interpret in solid-state
 302 reactions [38].

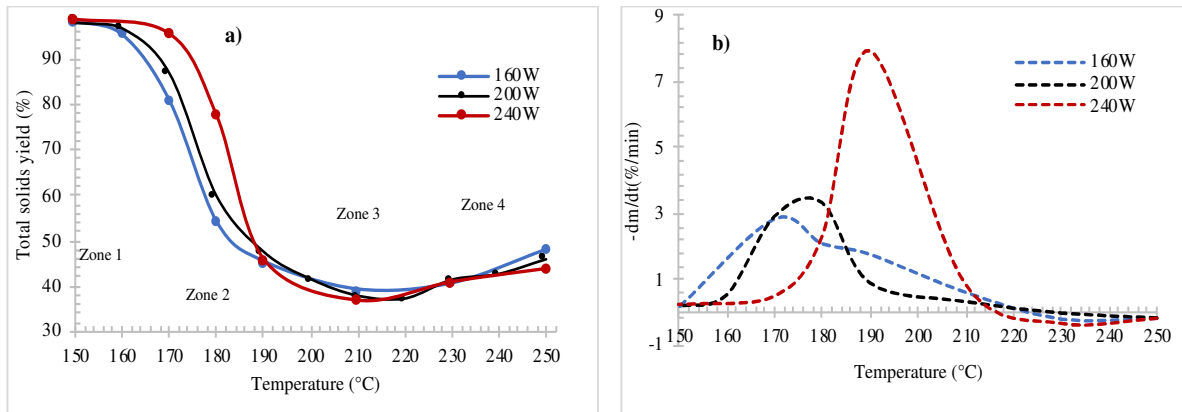
303 3 RESULTS AND DISCUSSION

304 3.1 Mass yield and derivative mass yield analysis

305 The Y_{HC} and DY_{HC} curves of the AS at different powers applied in the reactor corresponding to
306 different heating rates are shown in **Fig. 2a**. The evolution with the temperature at different
307 heating rates of Y_{HC} is calculated based on the **Eq.(1)** at different temperatures. Four distinct
308 zones can be identified in the **Fig. 2a**. Up to 160 °C, initial induction period is observed in which
309 the reaction rate is quite slow (first zone). In this period, the energy in the reaction medium is not
310 high enough to reach activation energy. The reaction starts in the second zone, at a temperature
311 of ~160 °C; in this zone, the maximum rate of biomass decomposition is observed, and it is
312 finished at approximately 200 °C.

313 This decrease in mass yield is due to decomposition reactions of biomasses, such as hydrolysis,
314 dehydration, decarboxylation, and so forth [41]. The hydrolysis breaks down the biomass
315 chemical structure through cleavage of ester and ether bonds of bio-macromolecules with water
316 molecules. This process creates (oligo-) saccharides and fragments of lignin that enter the liquid
317 phase [45, 46] thus reducing the total solid yield, as shown in **Fig. 2a**. The hydrolyzed products
318 can degrade into furfurals, particularly 5-hydroxymethylfurfural, aldehyde, erythrose, and with
319 undergo dehydration and decarboxylation [47]. Dehydration removes water from the biomass
320 matrix without changing its chemical constitution, evidenced by the increased carbon contents
321 and decreased oxygen contents. Decarboxylation involves the degradation of hemicellulose and
322 cellulose; these materials can degrade into monomers, such as acetic acid, formic acid, lactic
323 acid, and furfurals further degrade into CO_2 and H_2O [42]. The decarboxylation reaction removes
324 carboxyl and carbonyl groups. Carboxyl and carbonyl groups rapidly degrade above 150-180 °C,
325 yielding CO_2 , and CO , respectively [48]. All these reactions mentioned above are decomposition
326 reactions, causing a decrease in the total solid yield and increasing the liquid and gas production.
327 The low decomposition temperature of this biomass can be related to its high content of
328 hemicellulose (76.4%) or biomolecules with solubilities similar to that of hemicellulose. Other
329 reaction mechanisms of HTC are aromatization and polymerization. HTC increases the
330 production of aromatics from intermediates products formed during hydrolysis [42]. Moreover,
331 lignin is composed of many aromatic compounds polymerized by various linkages. Hydrochar
332 produced during HTC is a cross-linked polymer and has similar properties to lignin, so

333 hydrochar is almost impossible to distinguish from the unreacted lignin fraction. Also, a
334 polymer, such as cellulose and hemicellulose can be converted into a cross-linked polymer
335 similar to lignin [49, 50].



336

337 **Fig. 2:** Evolution with temperature, a) the total solids yield (Y_{HC}), b) and derivative of total solids yield
338 (DY_{HC}) at different power (160, 200 and 240W).

339 The stability of the aromatic structures is a basic element in the hydrochar formation. This
340 stability is observed in zone 3, between 200 and 220 °C, as shown in **Fig. 2a**. The intermediates
341 of unsaturated compounds such as aldehydes, furfural, and 5-HMF produced from dehydration
342 and decarboxylation reactions are highly reactive. These monomers are followed by
343 condensation, polymerization, and aromatization to form S-HC [5, 42]. The S-HC formation
344 increases the total solid yield, as shown in zone 4 in **Fig. 2a**, between 220 and 250 °C. Similar
345 increases of the total solid yield were observed by Yang et al. [51] during the cellulose
346 carbonization at a temperature above 275 °C. The inclusion of a stirrer in the reactor helps obtain
347 a uniform biomass/water mixture inside the reactor, avoiding concentration or temperature
348 gradients inside the reactor; this may increase the reaction mechanisms in the HTC process. The
349 increased reaction mechanism can lead to rapid polymerization of the intermediates of
350 unsaturated compounds produced from dehydration and decarboxylation.

351 The heating rate is an essential factor during the thermochemical conversion process of biomass
352 since it affects the process through a heat transfer and mass transfer through the biomass
353 particles. In the **Fig. 2**, the Y_{HC} and DY_{HC} are represented at various heating rates. However,

354 DY_{HC} curve (**Fig. 2b**) became sharper as the heating rate increased. Higher heating rates
355 significantly enhanced total solid yield loss rates than those by the lower heating rates.

356 **Fig. 2b** shows that the peaks of DY_{HC} curves slightly shifted to the right as the heating rate
357 increased this can be explained by the fact that the gradient temperature of a particle and
358 distribution of temperature was smaller at low heating rates. The maximum decomposition peaks
359 were observed of 174, 182, and 189 °C for a power of 160, 200, and 240 W, respectively.

360 **3.2 Secondary hydrochar analysis.**

361 The condensation, polymerization, and aromatization reactions form secondary hydrochar on the
362 surface of the primary hydrochar. This secondary hydrochar is derived from the decomposition
363 of hemicellulose, and cellulose, followed by polymerization of intermediates product into
364 amorphous carbonaceous compounds during HTC. The increase in temperature and time of HTC
365 gradually increases the amorphous carbon, such as aliphatic and aromatic groups on the surface
366 of the primary hydrochar [52]. The condensation of amorphous carbon on the primary hydrochar
367 surface during HTC results in the retention of PAHs [20]. This secondary hydrochar was
368 extracted from the total solids produced at 190, 210, 230, and 250 °C at a heating power of 1.5
369 °C/min by extracting Soxhlet with toluene (100%). Extraction was also done with raw biomass.
370 The amount extracted in the hydrochar structures and the raw biomass is presented in **Table 3**. It
371 was noteworthy to note that a significant increase in secondary hydrochar removed in total
372 solids produced was observed when the temperature was above 190 °C; this explains the increase
373 in total solid yield or total hydrochar as explained in **section 3.1, Fig. 2**. The analyses of liquid
374 solutions of secondary hydrochar and biomass extractive compounds show different aliphatic
375 and PAHs compounds.

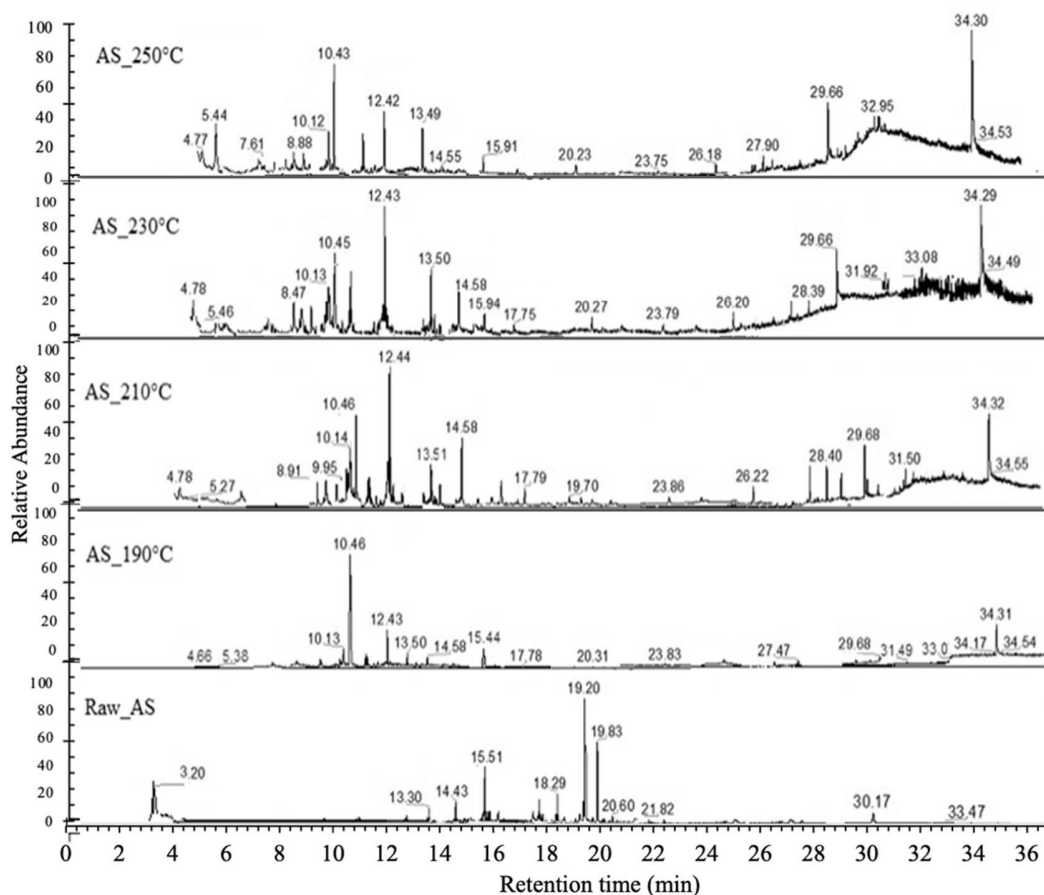
376 **Table 3:** The secondary hydrochar removed in total solids yield at different HTC temperatures.

HTC-Temperature	Extracted secondary hydrochar. (wt.%)
AS_250°C	19.01
AS_230°C	13.86
AS_210°C	10.05
AS_190°C	5.48
Raw_AS	3.80

377 **3.2.1 Aliphatic content analysis**

378 The long-chain aliphatic hydrocarbons that were found are shown in **Fig. 3**. During HTC, a
379 series of reactions of the coalification occurred. The oxygenated hydrocarbons are initially
380 converted to aliphatic (alkanes, olefins) and aromatics compounds and then transformed to
381 higher hydrocarbons and larger PAHs with a further increase in temperature [17]. The high
382 molecular weight hydrocarbons, which were found in the S-HC solution, include long chain
383 alkanes, such as tetradecane (RT \approx 8.9min), pentadecane (RT \approx 10.1min), hexadecane (RT \approx
384 11.3min), heptadecane (RT \approx 12.4min), octadecane (RT \approx 13.5min), and eicosane (RT \approx
385 14.6min). The signal of these aliphatic compounds increases with increasing temperature, and it
386 was not detected in the S-HC solution removed from the raw biomass.

387 The main olefin of high molecular weight detected was 9-octadecenoic acid (oleic acid), an 18-
388 carbon monounsaturated fatty acid (RT \approx 34.3min). Also, it was detected 9-octadecenamide
389 (RT \approx 29.7min), an amide derived from oleic fatty acid. All these compounds were detected in all
390 the hydrochars produced. The intensity of the peaks increases, with the increase of the
391 temperature, they confirm the formation of tars on the hydrochar structure. The condensation of
392 these aliphatic compounds on hydrochar surface results in retention of PAHs [20]. Unlike the
393 hydrochar produced, the components that were detected in the raw biomass extractable were
394 mainly fatty acids, such as stearic acid (RT \approx 19.20min) and (11E)-11-octadecenoic acid (RT \approx
395 19.83min).

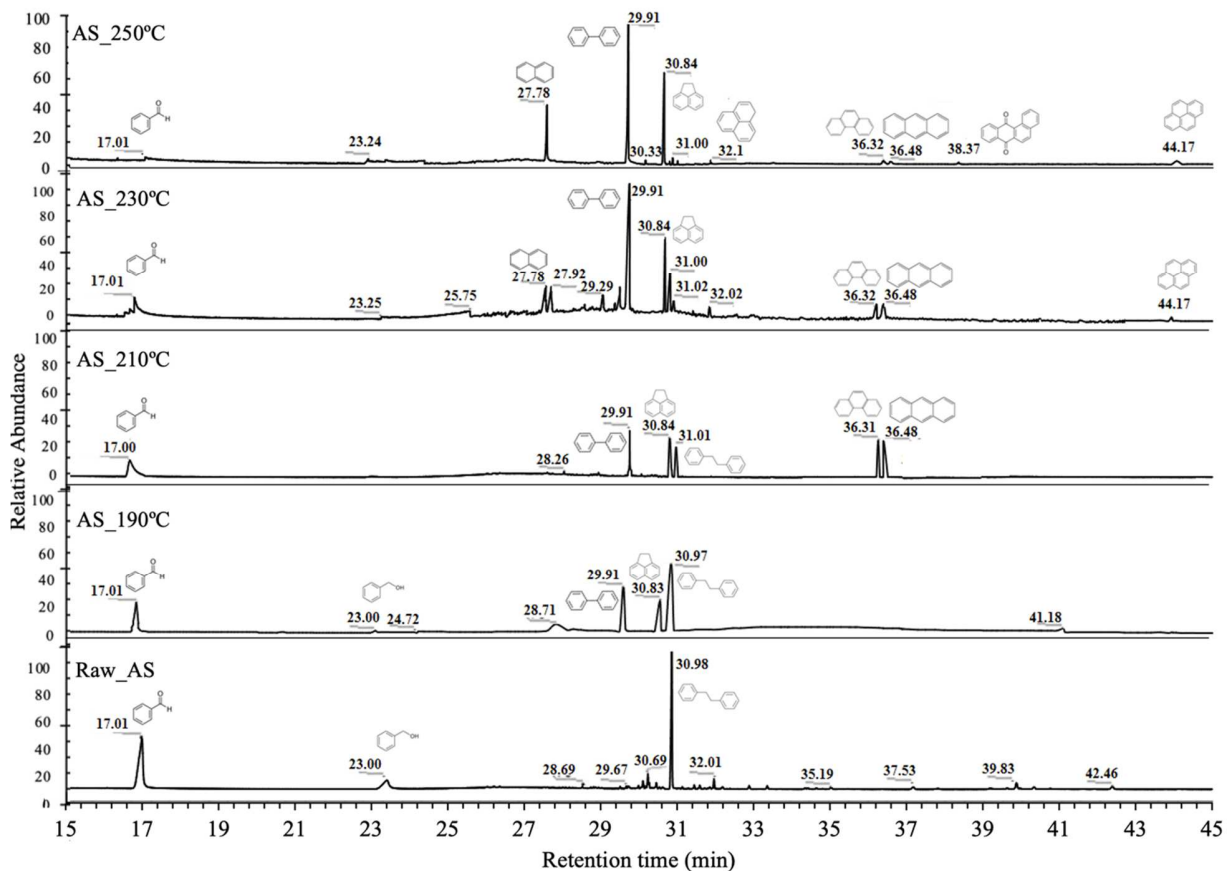


396

397 **Fig. 3:** The main aliphatic compounds detected in secondary hydrochar solution removed in the hydrochar
 398 structure and raw AS.

399 3.2.2 PAHs content analysis.

400 The chromatogram of total PAHs in hydrochar and raw AS are presented in **Fig. 4**. The results
 401 showed that total PAHs in the hydrochars were higher than those in raw AS. The PAHs detected
 402 in the raw biomass was bibenzyl (RT \approx 30.98min), the simplest PAHs (2 rings). The peak with a
 403 retention time of 17 and 23min are benzaldehyde and Benzyl alcohol, respectively. The number
 404 of PAHs detected in the hydrochars increases with increasing temperature; this may be explained
 405 by polymerization and aromatization reactions during the HTC process. At the lower temperature
 406 of HTC (190°C and 210°C), the PAHs detected were mainly 2-3 rings.



407
 408 **Fig. 4:** The main PAHs compounds detected in secondary hydrochar solution removed in the hydrochar
 409 structure and raw AS.

410 The 2-ring were biphenyl, bibenzyl, and naphthalene with the retention time of 29.91, 31 and
 411 27.78min respectively. The PAHs with 3 rings detected were acenaphthene, phenanthrene, and
 412 anthracene with retention times 30.84, 36.32, and 36.48min, respectively. In addition to the fact
 413 that all these mentioned PAHs were detected at a high temperature of HTC (230 and 250 °C),
 414 other PAHs were detected, such as 4-methyl biphenyl, acenaphthene, cis-stilbene, 1H-phenalene,
 415 and pyrene, with the retention time of 30.33, 31.07, 31.22 32.1, and 44.17 min respectively. At a
 416 temperature of 250°C, another 4-ring oxygenated PAHs was detected, such as 7,12-
 417 dihydrobenzo[a]anthracene, with the retention time of 38.37min. At low temperatures, the
 418 biomass was subjected to initial hydrolysis, dehydration, and depolymerization reaction [47],
 419 which led to a decrease in total PAHs because the polymerization and aromatization reaction
 420 have not started.. The intermediates unsaturated compounds produced from dehydration and
 421 decarboxylation promoted PAHs formation with increasing temperature by aromatization and

422 polymerization reactions, so increasing the PAHs rings formed. The hydrochars obtained at
 423 temperatures from 190 to 210 °C, biphenyl and bibenzyl (2 rings) were dominant while
 424 phenanthrene, Anthracene, and Pyrene were most prevalent at high HTC temperature (230 - 250
 425 °C).

426 3.3 Kinetic analysis results

427 Thermal analysis methods are currently used to determine the reactivities and mechanisms of
 428 thermal reactions of solids. Estimation of kinetic parameters involves activation energy and pre-
 429 exponential factor. This study proposes different model-free methods, such as FWO, KAS, and
 430 Friedman to determine AS kinetic parameters during HTC. Although model-free methods can
 431 reliably estimate the kinetic parameters, the information obtained is limited, It do not allow to
 432 define the reaction mechanism unlike model-fitting methods [53].

433 3.3.1 Model-free method

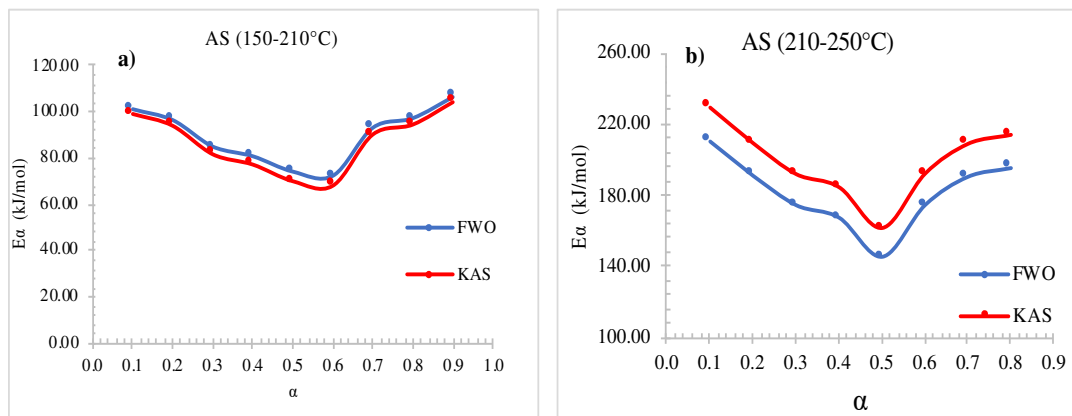
434 In this study, model-free methods first analyzed the kinetics of the HTC of AS. Starting from **Eq.**
 435 (5) and applying above mentioned isoconversional methods. The activation energy ($E\alpha$), pre-
 436 exponential factor (A), and linear correlation coefficient (R^2) at various conversion rates of 0.1–
 437 0.9 were calculated using the FWO, KAS, and Friedman methods. The calculated average values
 438 of $E\alpha$, A, and R^2 are shown in **Table 4**. These parameters were calculated in two zones of HTC
 439 temperature. The first zone corresponds to the decrease in the Y_{HC} between 150 and 210 °C, and
 440 the second zone corresponds to the increase of the Y_{HC} from 210 to 250 °C where appears
 441 formation of heavy PAHs

442 **Table 4:** Kinetic parameters of AS determined by the model-free kinetics methods.

Temperature (°C)	FWO			KAS			Friedman		
	$E\alpha$ (kJ/mol)	A (min ⁻¹)	R^2	$E\alpha$ (kJ/mol)	A (min ⁻¹)	R^2	$E\alpha$ (kJ/mol)	A (min ⁻¹)	R^2
150-210	89.61±12.19	7.55x10 ⁹	0.982	86.79±12.82	3.39x10 ⁹	0.979	73.81±35.47	2.24x10 ¹²	0.630
210-250	181.28±20.13	78x10 ⁻¹⁹	0.909	199.12±21.16	1.38x10 ⁻¹⁹	0.916	223.27±31.56	2.49x10 ⁻⁶	0.801

443 As shown in **Table 4**, the $E\alpha$ values obtained for the integral methods (FWO and KAS) are
 444 similar and show the best fit correlation coefficient (R^2) compared to the differential method
 445 (Friedman). The Friedman method requires derivative conversion data, which would lead to
 446 being numerically unstable and noise-sensitive [54]. For this reason, in general, the integral
 447 methods show the best-fit correlation coefficient values than the differential method.

448 In the first zone, the HTC temperatures were between 150 and 210 °C. The average E_a values
 449 were 89.61 ± 12.19 kJ/mol, 86.79 ± 12.82 kJ/mol. The small differences observed in E_a values
 450 obtained using KAS and FWO can be assigned to the different approximations of the
 451 temperature integral. In **Fig. 5a**, it can be observed that the values of E_a are not similar for all
 452 conversion values, indicating the existence of a complex multi-step mechanism reaction that
 453 occurs in the biomass HTC process. The progressive variation of E_a values could correspond to
 454 competitive or consecutive reactions and the multiphasic biomass conversion. For α values from
 455 0.1 to 0.6, a decrease of E_a from 99 to 68 kJ/mol. However, from 0.6, an increase of E_a is
 456 observed; this may be due to the change of the mechanism of chemical reactions. In this range of
 457 HTC temperature, similar values of E_a were reported by Killer et al. [26] for cellulose and
 458 hemicellulose using the nonlinear least-square minimization method. The values obtained were
 459 61 kJ/mol and 127 kJ/mol for hemicellulose and cellulose. Also, Danso-Boateng et al. [55]
 460 reported the value of activation energy (77.8 kJ/mol, with pre-exponential factor $1.5 \times 10^7 \text{ min}^{-1}$)
 461 for synthetic feces and 70.4 kJ/mol, with a pre-exponential factor of $4.0 \times 10^6 \text{ min}^{-1}$ for primary
 462 sewage sludge.



463
 464 **Fig. 5:** E_a values according to the degree of conversion (α) for HTC process of (a) 150 to 210 °C and (b)
 465 150 to 210 °C of HTC temperature according to the FWO and KAS.

466 In the second zone (210 to 250 °C), they corresponded to an increase in Y_{HC} for AS. The E_a
 467 values are displayed in **Table 4** and **Fig. 5b**. The values obtained are a similar trend for integral
 468 methods.

469 As in the previous one, there is also a change in the trend of E_a showing a complex multi-step
 470 mechanism reaction. The values of E_a vary from 145.28 to 210.74 kJ/mol and 245.28 to 229.95

471 kJ/mol for FWO and KAS respectively. As a comparison, the FWO and KAS method was more
 472 reliably attributed to its higher R^2 values. The high E_a values obtained in this temperature zone
 473 are due to the condensation, polymerization, and aromatization reactions. This reaction occurs at
 474 higher temperatures and reaction times [5]. In this temperature range (205-245 °C), Yang et al.
 475 [51] reported values of 226.5 kJ/mol of HTC for cellulose.

476 As shown in **Fig. 5**, the different E_a express different reaction mechanisms. The model-fitting
 477 methods can explain the different models for each stage of conversion.

478 3.3.2 Model-fitting method

479 The model-fitting method applied in this study was the Coats-Redfern method; this method
 480 enabled the determination of the kinetic parameters, i.e., activation energy and kinetic model
 481 ($g(\alpha)$). In **Table 5**, the average activation energy of different heating rates is displayed to identify
 482 the kinetic reaction model of the HTC process for AS. As shown in **Table 5**, the E_a values
 483 determined are somewhat mildly variable when changing the reaction model and can be really
 484 different to the value obtained with model-free method.

485 **Table 5:** Kinetic parameters of AS determined by model-fitting method in HTC process for AS

Model-Symbols	150-210°C		210-250°C	
	$E_{a\text{mean}}$ (kJ/mol)	R^2_{mean}	$E_{a\text{mean}}$ (kJ/mol)	R^2_{mean}
R1	148.84±4.93	0.968	230.96±28.84	0.916
R2	212.95±5.53	0.988	330.30±37.72	0.937
R3	292.87±6.57	0.977	453.89±48.76	0.928
R4	178.58±5.19	0.983	277.12±32.98	0.933
D1	214.92±8.94	0.909	329.16±44.61	0.853
D2	239.39±9.26	0.931	367.69±48.32	0.877
D3	270.92±9.55	0.953	417.00±52.85	0.902
D4	249.74±9.35	0.939	383.89±49.81	0.887
P1	159.32±6.70	0.907	244.76±33.45	0.85
P2	48.12±2.22	0.888	75.96±11.14	0.831
P3	29.59±1.48	0.87	47.83±7.42	0.813
P4	20.32±1.10	0.847	33.76±5.56	0.794
A1	96.73±3.28	0.966	151.16±19.22	0.913
A2	70.68±2.46	0.964	111.26±14.41	0.91
A3	44.63±1.64	0.96	71.36±9.60	0.903
A4	31.60±1.23	0.955	51.41±7.20	0.896
A5	101.75±2.32	0.903	161.50±16.08	0.87

A6	210.98±4.59	0.869	331.44±32.16	0.906
F1	48.12±2.22	0.888	75.96±11.14	0.831
F2	29.59±1.48	0.87	47.83±7.42	0.813

486 The main hypotheses that can explain the inconsistency $E\alpha$ values between the model-free and
 487 model-fitting methods are the model-free model assumes that the reaction mechanism is first-
 488 order. However, there may be different mechanisms during the conversion process. These
 489 mechanisms can be explained for the model-fitting. Also, to determine the kinetic parameter for
 490 model-free method, at least three heating rates are required. On the other hand, only one heating
 491 rate value is necessary for the model-fitting to estimate the kinetic parameters. In most biomass
 492 thermal degradation works in literature, the chosen kinetic model is the reaction first order
 493 ($f(\alpha)=1-\alpha$), even if each phase could be described as a different model. In this case, if the mean
 494 value of $E\alpha$ for different heating rates at a specified conversion range based upon one particular
 495 model is closest to the value by the model-free methods, in addition to the high correlation
 496 coefficients (R^2), then this model may dominate the reactions in this range [56, 57].

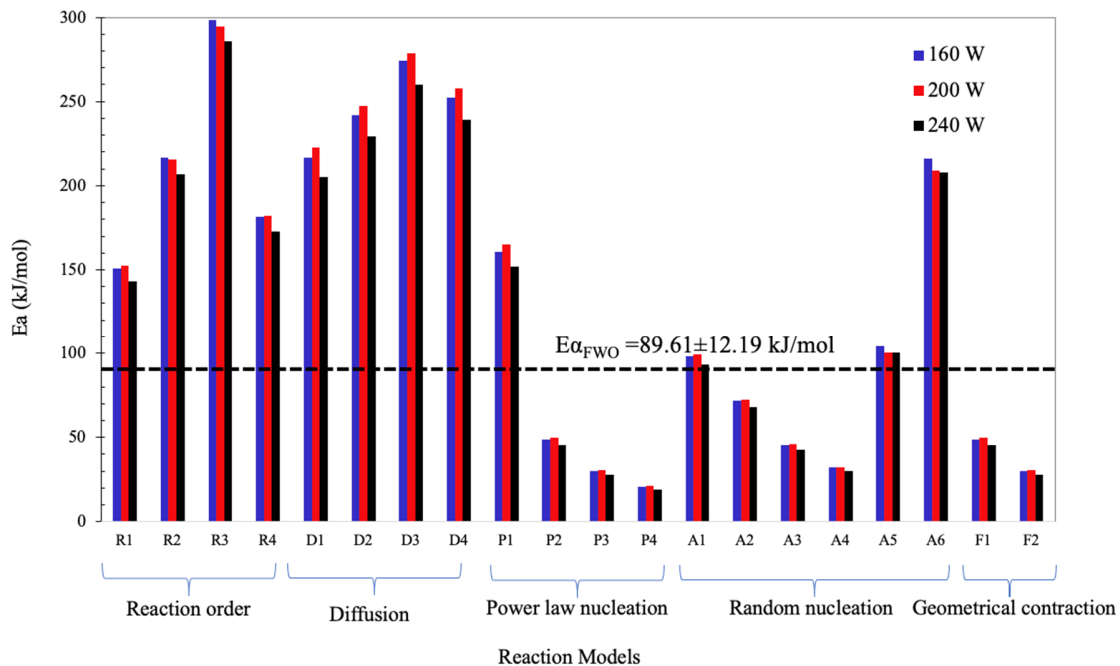
497 The calculated $E\alpha$ at different heating rates is shown in **Fig. 6** and **Fig. 7**. It can be seen in **Fig. 6**
 498 that for the reaction order model series, the estimated average value of $E\alpha$ for the cases of the
 499 three heating rates varies from 148.8 kJ/mol to 292.87kJ/mol. But none of the estimated average
 500 $E\alpha$ based upon this series reaction model is close to 89.61 kJ/mol. Although higher correlation
 501 values are obtained for this model series ($R^2 > 0.968$), the $E\alpha$ values obtained are much greater
 502 than those of the free models values.

503 In fact, the reaction model corresponding to Avrami-Erofeev (1) gives a similarity $E\alpha$ values
 504 with model-free methods in the temperature between 150 and 210°C indicate that the HTC
 505 kinetics of AS follows a random nucleation model ($g(\alpha) = [-\ln(1-\alpha)]^{2/3}$). The kinetic
 506 transformations of Avrami-Erofeev models usually follow a characteristic sigmoidal profile (S-
 507 shape) where the transformation rates are low at the beginning and the end of the transformation
 508 but rapid in between; this explains the shape of the curve in **Fig. 2a**. A similar observation was
 509 reported by Álvarez-Murillo et al. [58] in the HTC process for the cellulose decomposition
 510 curve.

511 However, in the second zone (210 to 250°C) corresponding to an increase in Y_{HC} , the best model
 512 giving the value close to $E\alpha_{FWO}$ (181.28 kJ/mol) is the first order model (R1) as shown in **Fig. 7**.
 513 The estimated average value of $E\alpha$ varies from 199.26 kJ/mol to 255.65 kJ/mol. The first-order

514 reaction model may be the most appropriate model to express the HTC process of AS in this
 515 temperature range.

516

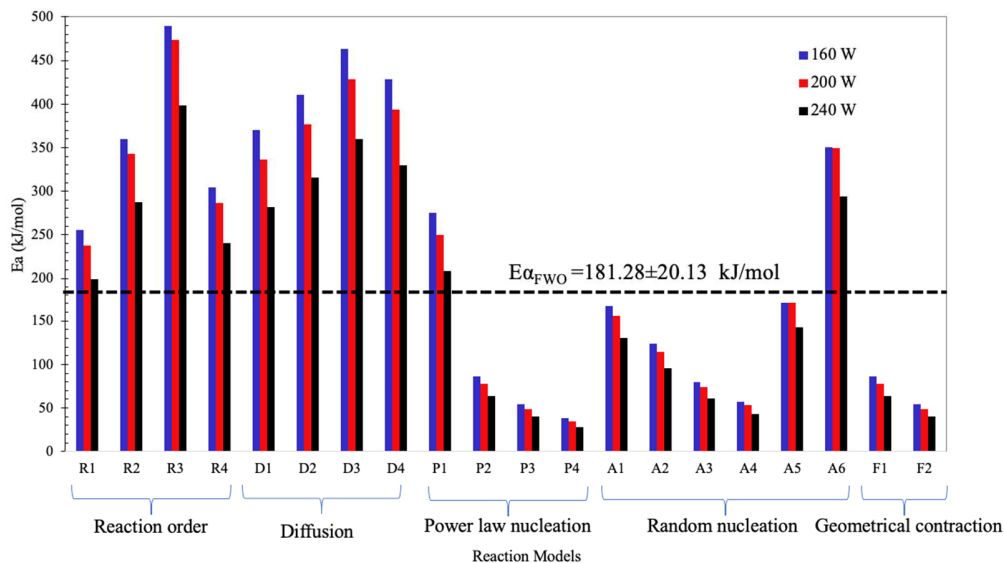


517

518 **Fig. 6:** Comparison of kinetic parameters from model-fitting methods of temperature between 150 and
 519 210°C

520 Although model-free methods were generally regarded as reliable ones, they can calculate both
 521 $E\alpha$ and A values. However, this method is based on supposed first-order reaction models, and the
 522 thermal decomposition can follow different reaction models, which are not necessarily first-order
 523 model reactions, as demonstrated for AS HTC temperature between 150 and 210 °C. On the
 524 other hand, model-fitting methods have enabled the determination of the kinetic model ($g(\alpha)$),
 525 also activation energy ($E\alpha$), but any list of the model-fitting method is certainly incomplete, and
 526 it is entirely possible that the studied process is not described by any of them [54].

527 Moreover, this method depends on the heating rate and range of conversion. As shown in **Fig. 7**,
 528 $E\alpha$ values increased with increasing heating rate. This phenomenon is because as the heating rate
 529 increased, it led to a sharp increase in intermediates reaction rates and lower activation energies.
 530 Similar results were observed by Mui et al. [59] in the pyrolysis of cellulose, hemicellulose, and
 531 lignin.



533

534 **Fig. 7:** Comparison of kinetic parameters from model-fitting methods of temperature between 210 and
535 250°C

536 Consequently, it was recommended that model-fitting methods and model-free methods support
537 each other to investigate the HTC mechanism. Therefore, according to comparing the model-free
538 and model-fitting methods' activation energy, the random nucleation (Avrami-Erofeev-1) model
539 may be considered the most suitable model to characterize the HTC of AS in the range of 150°C
540 to 210°C. Simultaneously, a temperature between 210 and 250°C follows a first-order reaction
541 model.

542 **Conclusions:**

543 This study is focused on kinetic studies of hydrothermal carbonization of avocado stone, using
544 different temperature and time conditions. The kinetics of the process was studied using different
545 models and methods (model-free and model-fitting methods). The following conclusions can be
546 drawn from the results of the study:

547 According to the analysis of total solids yield, the HTC of the AS can be divided into four main
548 zones. Initial induction period in the first zone in which the reaction rate is relatively slow (up to
549 160°C), followed by a maximum loss of total solid yield up to 200°C. The third zone corresponds
550 to the stabilization zone, dominated by condensation reactions; this stability is observed between
551 200 and 220°C. The last zone is the increase in the total solid mass yield. The increase of the

552 total solid mass yield between 220 and 250°C is related to the aromatization and polymerization
553 reactions. This increase was confirmed with the Soxhlet extraction and analysis of the secondary
554 hydrochars (tars) formed. The increase in temperature of HTC gradually increases the tars
555 compounds, such as aliphatic and PAHs on the hydrochar.

556 The results of GC–MS analysis of the secondary hydrochar solution indicate that it contains
557 aliphatic and PAHs components. The aliphatic compounds detected were mainly characterized
558 by long-chain alkanes and some unsaturated fatty acids. The number and weight of PAHs
559 increase with the increasing temperature of HTC. The most abundant PAHs were two and three-
560 ring. However, 4-ring PAHs were detected in low numbers in hydrochars produced at 230 and
561 250°C.

562 The decomposition of avocado stone during the HTC in temperatures range between 150 and
563 210°C follows a random nucleation reaction mechanism (Avrami-Erofeev-1) whereas in the
564 temperature between 210 and 250 follows a first-order reaction model. The average activation
565 energy estimated for Avrami-Erofeev-1 was 96.73 ± 3.28 kJ/mol. The values obtained from FWO
566 and KAS are consistent with Avrami-Erofeev-1, where the activation energies are 89.61 ± 12.19
567 kJ/mol and 86.79 ± 12.82 kJ/mol, respectively. The average activation energy estimated for the
568 first-order reaction model is 230.96 ± 28.84 kJ/mol. The best values obtained for the model-free
569 method were between 145-210 kJ/mol and 161-229 kJ/mol for the FWO and KAS methods.
570 Moreover, the values of activation energies at different conversions have indicated the multi-
571 reaction scheme's existence during the HTC of avocado stone.

572 **Acknowledgments**

573 The authors are grateful to CONACYT (Consejo Nacional de Ciencia y Tecnología de México)
574 for granting the scholarship No. 659624 for this research. Also, we are grateful to ICARE -
575 CNRS- France and the Région Centre-Val de Loire for financial support within the INFLUX
576 project.

577

578 **References**

- 579 1. Czernik S, Bridgwater A. Overview of applications of biomass fast pyrolysis oil. *Energy & fuels*
580 2004; **18**(2): 590-598
- 581 2. Funke A, Ziegler F. Hydrothermal carbonization of biomass: a summary and discussion of
582 chemical mechanisms for process engineering. *Biofuels, Bioproducts and Biorefining* 2010; **4**(2):
583 160-177

- 584 3. Kim D, Lee K, Park K Y. Hydrothermal carbonization of anaerobically digested sludge for solid
585 fuel production and energy recovery. *Fuel* 2014; **130**: 120-125
- 586 4. Missaoui A, Bostyn S, Belandria V, Cagnon B, Sarh B, et al. Hydrothermal carbonization of
587 dried olive pomace: Energy potential and process performances. *Journal of Analytical and*
588 *Applied Pyrolysis* 2017
- 589 5. Sevilla M, Fuertes A B. The production of carbon materials by hydrothermal carbonization of
590 cellulose. *Carbon* 2009; **47**(9): 2281-2289
- 591 6. Sabio E, Álvarez-Murillo A, Román S, Ledesma B. Conversion of tomato-peel waste into solid
592 fuel by hydrothermal carbonization: Influence of the processing variables. *Waste management*
593 2016; **47**: 122-132
- 594 7. Chen W-H, Ye S-C, Sheen H-K. Hydrothermal carbonization of sugarcane bagasse via wet
595 torrefaction in association with microwave heating. *Bioresource technology* 2012; **118**: 195-203
- 596 8. Zhang L, Liu S, Wang B, Wang Q, Yang G, et al. Effect of residence time on hydrothermal
597 carbonization of corn cob residual. *BioResources* 2015; **10**(3): 3979-3986
- 598 9. Álvarez-Murillo A, Román S, Ledesma B, Sabio E. Study of variables in energy densification of
599 olive stone by hydrothermal carbonization. *Journal of Analytical and Applied Pyrolysis* 2015;
600 **113**: 307-314
- 601 10. Alves B. Fresh avocado production in Mexico from 2013/14 to 2019/20. 2020; Available from:
602 <https://www.statista.com/statistics/591329/mexico-fresh-avocado-production/>
- 603 11. Perea-Moreno A-J, Aguilera-Ureña M-J, Manzano-Agugliaro F. Fuel properties of avocado stone.
604 *Fuel* 2016; **186**: 358-364
- 605 12. Salgado J M, Danieli F, Regitano-D'Arce M A B, Frias A, Mansi D N. The Avocado Oil (persea
606 Americana Mill) As A Raw Material For The Food Industry [o óleo De Abacate (persea
607 Americana Mill) Como Matéria-prima Para A Indústria Alimentícia]. *Ciencia e Tecnologia de*
608 *Alimentos* 2008
- 609 13. Rodríguez-Sánchez D G, Pacheco A, García-Cruz M I, Gutiérrez-Urbe J A, Benavides-Lozano J
610 A, et al. Isolation and structure elucidation of avocado seed (*Persea americana*) lipid derivatives
611 that inhibit *Clostridium sporogenes* endospore germination. *Journal of agricultural and food*
612 *chemistry* 2013; **61**(30): 7403-7411
- 613 14. McLeod L, Flores D. USDA-Foreign-Agricultural-Service (2017) Mexico Avocado Annual. 2017
614 [cited 2020 25/10]; Available from: <https://www.fas.usda.gov/data/mexico-avocado-annual-2>
- 615 15. Lucian M, Volpe M, Gao L, Piro G, Goldfarb J L, et al. Impact of hydrothermal carbonization
616 conditions on the formation of hydrochars and secondary chars from the organic fraction of
617 municipal solid waste. *Fuel* 2018; **233**: 257-268
- 618 16. Paksung N, Pfersich J, Arauzo P J, Jung D, Kruse A. Structural effects of cellulose on hydrolysis
619 and carbonization behavior during hydrothermal treatment. *ACS omega* 2020; **5**(21): 12210-
620 12223
- 621 17. Peng N, Li Y, Liu T, Lang Q, Gai C, et al. Polycyclic aromatic hydrocarbons and toxic heavy
622 metals in municipal solid waste and corresponding hydrochars. *Energy & Fuels* 2017; **31**(2):
623 1665-1671
- 624 18. Wang L, Li A, Chang Y. Hydrothermal treatment coupled with mechanical expression at
625 increased temperature for excess sludge dewatering: Heavy metals, volatile organic compounds
626 and combustion characteristics of hydrochar. *Chemical Engineering Journal* 2016; **297**: 1-10

- 627 19. Malghani S, Gleixner G, Trumbore S E. Chars produced by slow pyrolysis and hydrothermal
628 carbonization vary in carbon sequestration potential and greenhouse gases emissions. *Soil*
629 *Biology and Biochemistry* 2013; **62**: 137-146
- 630 20. Al-Wabel M I, Rafique M I, Ahmad M, Ahmad M, Hussain A, et al. Pyrolytic and hydrothermal
631 carbonization of date palm leaflets: Characteristics and ecotoxicological effects on seed
632 germination of lettuce. *Saudi journal of biological sciences* 2019; **26**(4): 665-672
- 633 21. Wang T, Zhai Y, Zhu Y, Li C, Zeng G. A review of the hydrothermal carbonization of biomass
634 waste for hydrochar formation: Process conditions, fundamentals, and physicochemical
635 properties. *Renewable and Sustainable Energy Reviews* 2018; **90**: 223-247
- 636 22. Zeng X, Ueki Y, Yoshiie R, Naruse I, Wang F, et al. Recent progress in tar removal by char and
637 the applications: A comprehensive analysis. *Carbon Resources Conversion* 2020; **3**: 1-18.
- 638 23. Kambo H S, Dutta A. A comparative review of biochar and hydrochar in terms of production,
639 physico-chemical properties and applications. *Renewable and Sustainable Energy Reviews* 2015;
640 **45**: 359-378
- 641 24. Ischia G, Fiori L. Hydrothermal Carbonization of Organic Waste and Biomass: A Review on
642 Process, Reactor, and Plant Modeling. *Waste and Biomass Valorization* 2021; **12**(6): 2797-2824
- 643 25. Reza M T, Yan W, Uddin M H, Lynam J G, Hoekman S K, et al. Reaction kinetics of
644 hydrothermal carbonization of loblolly pine. *Bioresource technology* 2013; **139**: 161-169
- 645 26. Keiller B G, Muhlack R, Burton R A, van Eyk P J. Biochemical Compositional Analysis and
646 Kinetic Modeling of Hydrothermal Carbonization of Australian Saltbush. *Energy & Fuels* 2019;
647 **33**(12): 12469-12479
- 648 27. Liu Z, Balasubramanian R. Hydrothermal carbonization of waste biomass for energy generation.
649 *Procedia Environmental Sciences* 2012; **16**: 159-166
- 650 28. Pecchi M, Patuzzi F, Benedetti V, Di Maggio R, Baratieri M. Kinetic analysis of hydrothermal
651 carbonization using high-pressure differential scanning calorimetry applied to biomass. *Applied*
652 *Energy* 2020; **265**: 114810
- 653 29. Ceballos A M, Montoya S. Evaluación química de la fibra en semilla, pulpa y cáscara de tres
654 variedades de aguacate. *Biotecnología en el sector agropecuario y agroindustrial* 2013; **11**(1):
655 103-112
- 656 30. Sangare D, Missaoui A, Bostyn S, Belandria V, Moscosa-Santillan M, et al. Modeling of Agave
657 Salmiana bagasse conversion by hydrothermal carbonization (HTC) for solid fuel combustion
658 using surface response methodology. *aimspress energy* 2020; **8**(4): 538-562
- 659 31. Sangare D, Bostyn S, Moscosa-Santillan M, Gökalp I. Hydrodynamics, heat transfer and kinetics
660 reaction of CFD modeling of a batch stirred reactor under hydrothermal carbonization conditions.
661 *Energy* 2020: 119635
- 662 32. Román S, Libra J, Berge N, Sabio E, Ro K, et al. Hydrothermal carbonization: modeling, final
663 properties design and applications: a review. *Energies* 2018; **11**(1): 216
- 664 33. Hilber I, Blum F, Leifeld J, Schmidt H-P, Bucheli T D. Quantitative determination of PAHs in
665 biochar: a prerequisite to ensure its quality and safe application. *Journal of agricultural and food*
666 *chemistry* 2012; **60**(12): 3042-3050
- 667 34. Mumbach G D, Alves J L F, da Silva J C G, Di Domenico M, de Sena R F, et al. Pyrolysis of
668 cocoa shell and its bioenergy potential: evaluating the kinetic triplet, thermodynamic parameters,
669 and evolved gas analysis using TGA-FTIR. *Biomass Conversion and Biorefinery* 2020: 1-17

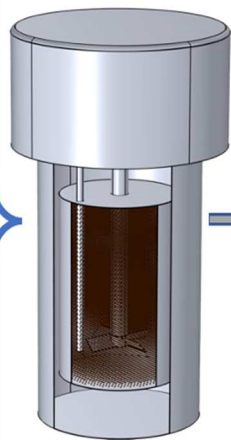
- 670 35. Doyle C D. Kinetic analysis of thermogravimetric data. *Journal of applied polymer science* 1961;
671 5(15): 285-292
- 672 36. Coats A, Redfern J. Kinetic parameters from thermogravimetric data. *Nature* 1964; **201**(4914):
673 68-69
- 674 37. Yao Z, Yu S, Su W, Wu W, Tang J, et al. Kinetic studies on the pyrolysis of plastic waste using a
675 combination of model-fitting and model-free methods. *Waste Management & Research* 2020;
676 **38**(1_suppl): 77-85
- 677 38. Qiu Y, Chen Y, Zhang G G, Yu L, Mantri R V, Developing solid oral dosage forms:
678 pharmaceutical theory and practice, in *Book Developing solid oral dosage forms: pharmaceutical
679 theory and practice*. 2016, Academic press
- 680 39. Khawam A, Flanagan D R. Solid-state kinetic models: basics and mathematical fundamentals.
681 *The journal of physical chemistry B* 2006; **110**(35): 17315-17328
- 682 40. Brown M E, Dollimore D, Galwey A K, Reactions in the solid state, in *Book Reactions in the
683 solid state*. 1980, Elsevier
- 684 41. Volpe M, Goldfarb J L, Fiori L. Hydrothermal carbonization of *Opuntia ficus-indica* cladodes:
685 Role of process parameters on hydrochar properties. *Bioresource technology* 2018; **247**: 310-318
- 686 42. Reza M T, Uddin M H, Lynam J G, Hoekman S K, Coronella C J. Hydrothermal carbonization of
687 loblolly pine: reaction chemistry and water balance. *Biomass Conversion and Biorefinery* 2014;
688 **4**(4): 311-321
- 689 43. Galwey A K, Brown M E, Thermal decomposition of ionic solids: chemical properties and
690 reactivities of ionic crystalline phases, in *Book Thermal decomposition of ionic solids: chemical
691 properties and reactivities of ionic crystalline phases*. 1999, Elsevier
- 692 44. Khawam A. Application of solid-state kinetics to desolvation reactions. *The journal of physical
693 chemistry B* 2007; **210**(37): 1520-1545
- 694 45. Fang J, Zhan L, Ok Y S, Gao B. Minireview of potential applications of hydrochar derived from
695 hydrothermal carbonization of biomass. *Journal of Industrial and Engineering Chemistry* 2018;
696 **57**: 15-21
- 697 46. Gao P, Zhou Y, Meng F, Zhang Y, Liu Z, et al. Preparation and characterization of hydrochar
698 from waste eucalyptus bark by hydrothermal carbonization. *Energy* 2016; **97**: 238-245
- 699 47. Krylova A Y, Zaitchenko V. Hydrothermal carbonization of biomass: a review. *Solid Fuel
700 Chemistry* 2018; **52**(2): 91-103
- 701 48. Peterson A A, Vogel F, Lachance R P, Fröling M, Antal Jr M J, et al. Thermochemical biofuel
702 production in hydrothermal media: a review of sub-and supercritical water technologies. *Energy
703 & Environmental Science* 2008; **1**(1): 32-65
- 704 49. Reza M T, Upgrading biomass by hydrothermal and chemical conditioning. 2013, University of
705 Nevada, Reno.
- 706 50. Reza M T, Andert J, Wirth B, Busch D, Pielert J, et al. Hydrothermal carbonization of biomass
707 for energy and crop production. *Applied Bioenergy* 2014; **1**(1): 11-29
- 708 51. Yang W, Shimanouchi T, Wu S, Kimura Y. Investigation of the degradation kinetic parameters
709 and structure changes of microcrystalline cellulose in subcritical water. *Energy & fuels* 2014;
710 **28**(11): 6974-6980

- 711 52. Jaruwat D, Udomsap P, Chollacoop N, Fuji M, Eiad-ua A. Effects of hydrothermal temperature
712 and time of hydrochar from Cattail leaves. in AIP Conference Proceedings. 2018. AIP Publishing
713 LLC
- 714 53. Ali I, Naqvi S R, Bahadar A. Kinetic analysis of Botryococcus braunii pyrolysis using model-free
715 and model fitting methods. Fuel 2018; **214**: 369-380
- 716 54. Cai J, Xu D, Dong Z, Yu X, Yang Y, et al. Processing thermogravimetric analysis data for
717 isoconversional kinetic analysis of lignocellulosic biomass pyrolysis: Case study of corn stalk.
718 Renewable and Sustainable Energy Reviews 2018; **82**: 2705-2715
- 719 55. Danso-Boateng E, Holdich R, Shama G, Wheatley A D, Sohail M, et al. Kinetics of faecal
720 biomass hydrothermal carbonisation for hydrochar production. Applied energy 2013; **111**: 351-
721 357
- 722 56. Chen R, Lu S, Zhang Y, Lo S. Pyrolysis study of waste cable hose with
723 thermogravimetry/Fourier transform infrared/mass spectrometry analysis. Energy Conversion and
724 Management 2017; **153**: 83-92
- 725 57. Pan L, Jiang Y, Wang L, Xu W. Kinetic study on the pyrolysis of medium density fiberboard:
726 Effects of secondary charring reactions. Energies 2018; **11**(9): 2481
- 727 58. Álvarez-Murillo A, Sabio E, Ledesma B, Román S, González-García C. Generation of biofuel
728 from hydrothermal carbonization of cellulose. Kinetics modelling. Energy 2016; **94**: 600-608
- 729 59. Mui E L, Cheung W, Lee V K, McKay G. Kinetic study on bamboo pyrolysis. Industrial &
730 engineering chemistry research 2008; **47**(15): 5710-5722
- 731
- 732

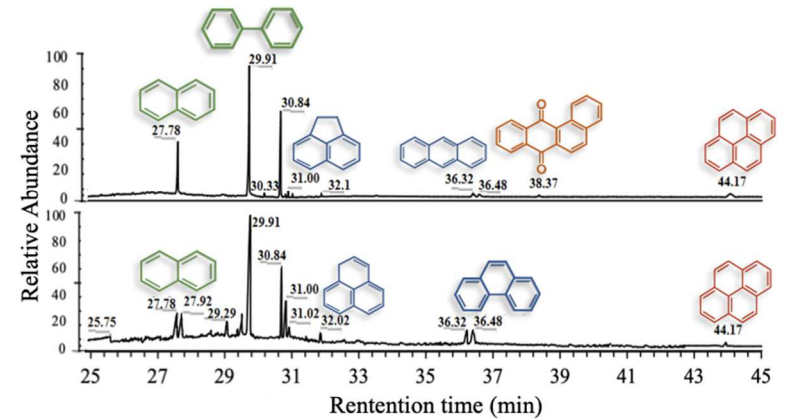
Graphical abstract



HTC Reactor



Hydrochar



PAHs compounds detected in the tar removed in the hydrochar

